Flexible Organic Electronic Ion Pump Fabricated Using Inkjet Printing and Microfabrication for Precision In Vitro Delivery of Bupivacaine

Dennis Cherian, Arghyamalya Roy, Alex Bersellini Farinotti, Tobias Abrahamsson, Theresia Arbring Sjöström, Klas Tybrandt, David Nilsson, Magnus Berggren, Camilla I. Svensson, David Poxson and Daniel Simon

LiU LINKÖPING UNIVERSITY

Flexible organic electronic ion pump fabricated using inkjet printing and microfabrication for precision *in vitro* delivery of bupivacaine

Dennis Cherian[1], Arghyamalya Roy[1], Alex Bersellini Farinotti[2] , Tobias Abrahamsson[1], Theresia Arbring Sjöström[1], Klas Tybrandt[1], David Nilsson[3], Magnus Berggren[1], Camilla I. Svensson[2]*, David J. Poxson[1], Daniel T. Simon[1]*

[1] Laboratory of Organic Electronics, Department of Science and Technology, Linköping University, 60174 Norrköping, Sweden

[2] Department of Physiology and Pharmacology, Karolinska Institutet, 17177 Stockholm, Sweden

[3] Unit of Printed Electronics, RISE Research Institutes of Sweden, Norrköping, Swede

E-mail: daniel.simon@liu.se, camilla.svensson@ki.se

Keywords: bioelectronics, inkjet printing, polyelectrolytes, flexible devices, polyimide

Abstract

The organic electronic ion pump (OEIP) is an on-demand electrophoretic drug delivery device, that via electronic to ionic signal conversion enables drug delivery without additional pressure or volume changes. The fundamental component of OEIPs is their polyelectrolyte membranes which are shaped into ionic channels that conduct and deliver ionic drugs, with high spatiotemporal resolution. The patterning of these membranes is essential in OEIP devices and is typically achieved using laborious micro processing techniques. Here, we report the development of an inkjet printable formulation of polyelectrolyte, based on a custom anionically functionalized hyperbranched polyglycerol (i-AHPG). This polyelectrolyte ink greatly simplifies the fabrication process, and is used in the production of free standing, OEIPs on flexible polyimide substrates. Both i-AHPG and the OEIP devices are characterized, exhibiting favorable iontronic characteristics of charge selectivity and ability to transport aromatic compounds. Further, the applicability of these technologies is demonstrated by transport and delivery of the pharmaceutical compound bupivacaine to dorsal root ganglion cells with high spatial precision and effective nerve-blocking, highlighting the applicability of these technologies for biomedical scenarios.

1. Introduction

Biological systems use highly complex ionic transport for signaling and communication. As such, there is an ongoing concerted effort to develop technologies capable of directly interacting with life's ionic systems[1,2]. Recently, a special class of organic electronic devices, known as iontronics, is being investigated for their capability to bridge the electronic–ionic gap separating electronic and living systems. Iontronic devices accomplish this translation between electronic and ionic signals by converting the flow of electrons to the transport and delivery of atomic ions[3] and even small molecules[4]. The potential of such iontronic devices has already been demonstrated in a variety of *in vivo* and *in vitro* biological scenarios, including drug delivery devices for seizure control[5], application in targeted chemotherapy[6], and even regulating plant physiology[7]. One of the fundamental technologies of iontronic devices that facilitates the regulated transport of ionic molecules is known as the organic electronic ion pump (OEIP). Currently, there is a growing development of iontronic devices utilizing a range of shapes and geometries including planar[8], free standing[9], capillary[4], and microfluidic-iontronic hybrid devices[10,11].

Common to all varieties of OEIPs is their incorporation of ionically conducting polymers, known as polyelectrolytes (PE), to achieve their distinctive capability of electrophoretic charge selective transport and delivery of ionic substances with high spatial resolution[12–14]. Selective ionic transport is accomplished through the ionically conducting PE enabled by the presence of a high fixed charge concentration anchored to the PE membrane itself[15]. The polarity of the PE membrane determines the

polarity of charge that can be transported, cations requiring a cation exchange membrane (CEM), and anions requiring an anion exchange membrane (AEM).

For the ambitions of iontronics to be fully realized, ultimately the devices and materials employed must meet the sophistication and complexity demands of the biological environments. Thus, continued development of iontronic components with sophisticated and miniaturized device architectures as well as their incorporation with other technologies is necessary. These demands point towards a key limitation of the current generation of fabrication of iontronic PE membranes which often necessitate the use of cleanroom processing techniques such as spin coating, photolithographic patterning, and lift off or etching techniques[3,16–18]. While these traditional microfabrication methods typically enjoy excellent device feature resolution, they also generally constrain the device architecture by requiring overall compatibility with often stringent processing and material requirements that must be simultaneously balanced, *e.g.*, high temperature requirements for curing, chemical compatibility between different layers. Furthermore, many of these fabrication techniques require the substrates and materials to be chemically inert with the developing solvents and that they should be able to withstand high temperature curing and exposure to high vacuum during thermal evaporation and etching. As such, micro-processing conditions can greatly constrain the potential form factor OEIP technologies may take; specifically, limitations related to the geometry and type of substrate of the device. Additionally, while high resolution and throughput can be achieved using micro-processing, in the laboratory setting, such techniques often require several sequential processing steps making device fabrication time and labor intensive. Lastly, traditional micropatterning of PE membranes is often subtractive in nature and can suffer from high material consumption, which may be a particularly relevant factor in the research setting when using specialized materials synthesized in small quantities.

One technique that can help address the limitations of micro-processing of PE membranes is the well-known method of inkjet printing. Because inkjet printing is a non-contact fabrication method, the additive mask-less manufacturing approach can greatly simplify fabrication protocols, reduce material waste, and avoid potentially undesirable processing environments (chemical, temperature, vacuum). Inkjet printing has already found interesting and promising applications in thin film transistors[19], diodes[20], printed circuitry[21], sensors[22] to biological and pharmaceutical applications[23], and even 3D printing techniques[24]. Ultimately, inkjet printing of PE membranes opens the door to a greater range of device architectures and applications.

Here, we detail the expansion of OEIP processing capabilities through the development of an inkjettable PE membrane and the realization of a free-standing hybrid inkjet printed and micropatterned OEIP. The PE ink formulation reported here (i-AHPG) utilizes the recently reported polyelectrolyte material ("dendrolyte") based on hyperbranched polyglycerols (HPG). Charge functionalized HPG is a dendritic ion conducting polyelectrolyte that is tailor made for iontronic devices. Both cationically (CHPG) or anionically (AHPG) functionalized HPG PE membranes have been demonstrated[4,7][25][26]. Unlike the more traditional polyelectrolytes fabricated from linear polymer chains, such as polystyrenesulfonate (PSS)[8], PSS-co-maleic acid (PSS-co-MA)[27], and poly(vinylbenzyl chloride) quaternized by triphenylphospine (PVBPPh$_3$)[28], PE membranes of HPG materials have demonstrated the capability to transport larger ions with cyclic or aromatic structures (*e.g.*, indigo carmine[4], 466 g/mol).[25] Inkjet formulation and fabrication procedures are discussed in detail. We subsequently utilize the capability a HPG PE membrane to demonstrate the delivery of the pharmaceutical compound bupivacaine (343 g/mol), an analgesic nerve blocker that reversibly binds primarily to sodium channels[29,30] and prevents depolarization and subsequent, or downstream, nerve signaling. Additionally, an *in vitro* protocol developed using inkjet-OEIPs for high precision delivery of bupivacaine to live dorsal root ganglion (DRG) neurons is demonstrated.

2. Results and Discussions

2.1 Inkjet printing AHPG

In the process of inkjet printing, the nature of the printed pattern is determined by various factors, including the ink formulation, the inkjet parameters, the target substrate material and treatments, and the

physical parameters of the print environment. Here, we discuss the factors considered and optimized to achieve a high-quality inkjettable formulation of AHPG based polyelectrolyte.

In inkjet printing, liquid droplets are dispensed by piezoelectric deformation of the ink chamber. In addition to the electrical voltages applied, the primary physical properties determining an ink droplet's formation are the surface tension and viscosity. The first property, surface tension, indicates whether the molecules in the bulk fluid of the ink have lower energy than that of the print surface. The second property, viscosity, is a measure of the internal friction between the molecules in the bulk fluid of the ink, and hence determines the resistance of liquid flow through the nozzle.[31] After the formation of a droplet from the nozzle, it will fall under the influence of gravitational and aerodynamic forces to the substrate. Once the ink droplet is in free fall, it will form the shape with the lowest energy, *i.e.*, spherical. If during dispensing the properties of surface tension and viscosity are not well matched, ink-tails extending from the "cap" of the ink droplet can be produced, as well as additional so-called satellite droplets. Both ink-tails and satellite droplets can affect the overall quality of print[31–35]. Once the droplet contacts the substrate, each droplet spreads. If spaced sufficiently close, the spreading droplets coalesce with the previous droplets in the process of layer formation. While surface tension and viscosity primarily determine the properties of the droplet, other physical properties become important as well when determining the resulting ink pattern on the print surface. Ink to substrate interactions (dependent on the surface energy of the ink and substrate) predominantly influence the layer formation.[33] For polymer-based materials, other factors to be considered are particle size and boiling point of the mixture of solvents. To ensure that the particulate size in the ink is less than the nozzle diameter, all the solvents and polymers should be well mixed, ideally without any phase separation. An ink formulation's print behavior is also highly dependent on the solvents that are used to formulate the ink. The boiling point (b.p.) of the mixture should also be sufficiently high to avoid evaporation during droplet formation (*i.e.*, as the ink is expelled from the nozzle and is exposed to the ambient environment). Excessive evaporation can lead to residue on jet nozzles, resulting in clogging or uneven print performance.

AHPG is a dendritic polyelectrolyte material (dendrolyte), having hyperbranched polyglycerol as the core polymeric structure, functionalized with sulfonate as the anionic charge component and unsaturated allyl groups as available polymerizable/cross-linking group.[25] These materials allow ratios of the charge and cross-linking groups to be tuned during synthesis. The ink developed here, termed i-AHPG, consists of the base AHPG material combined with five additional components: methanol, deionized water, Thiocure ETTMP 1300 (ethoxylated trimethylolpropane tri (3-mercaptopropionate), 1300 g/mol), Irgacure 2959 (2-hydroxy-4-(2-hydroxyethoxy)-2-methylpropiophenone), and Nuosperse 2008, a commercial anionic organic polymeric surfactant. These components were mixed in a specific ratio (AHPG 25 wt%, methanol 39 wt%, water 29 wt%, Thiocure 5 wt%, Irgacure 0.5 wt%, and surfactant 1.5 wt%) to obtain ink within the requirements of the inkjet printing process. The primary solvent, DI water, has a surface tension of 72.2 mN/m[36] which when used alone, is too high for inkjet printing of AHPG (optimal range 28–32 mN/m for the inkjet cartridge we used[37]). Thus, methanol which has a surface tension of 22.7 mN/m[38], was used as a co-solvent to reduce the surface tension of the ink, improving the drop formation. By utilizing a high and low b.p. solvent (DI water 100 °C, methanol 64.7 °C) it was found that nozzle clogging could be avoided by ensuring the nozzle remained wet and ensuring no undesirable drying of the ink during dispensing. The primary function of Thiocure is as a crosslinking agent. Thiocure is liquid at room temperature and has a viscosity of 400 cp, thus it also functions as a viscosity modifier. Irgacure is used as a radical photo initiator for the AHPG at low wt%, and when fully dissolved had little influence on the physical properties of the i-AHPG ink. The liquid anionic polymeric surfactant also further reduced the ink solution's surface tension.

Droplet formation at the nozzle was monitored during print using the printer's built-in high resolution video camera and a representative picture of an i-AHPG ink droplet is shown in Figure 1a, taken at 400 μm from the print head. The droplets formed with a spherical cap, followed by a tail without satellite drops. From droplet image sequences, the velocity of the droplets as they reach the substrate surface (substrate was kept at 400 μm from print head) was calculated to be 5 m/s (from the image at 80 μs, when the drop reaches 400 μm). This velocity has been reported to be optimum for good droplet spread on the substrate.[39] These image sequences also showed that the formulated ink was prone to nozzle clogging during printing at room temperature. Precise control of the nozzle temperature is crucial in the inkjet printing of functional inks to avert nozzle clogging. Altering the temperature can lower the ink's
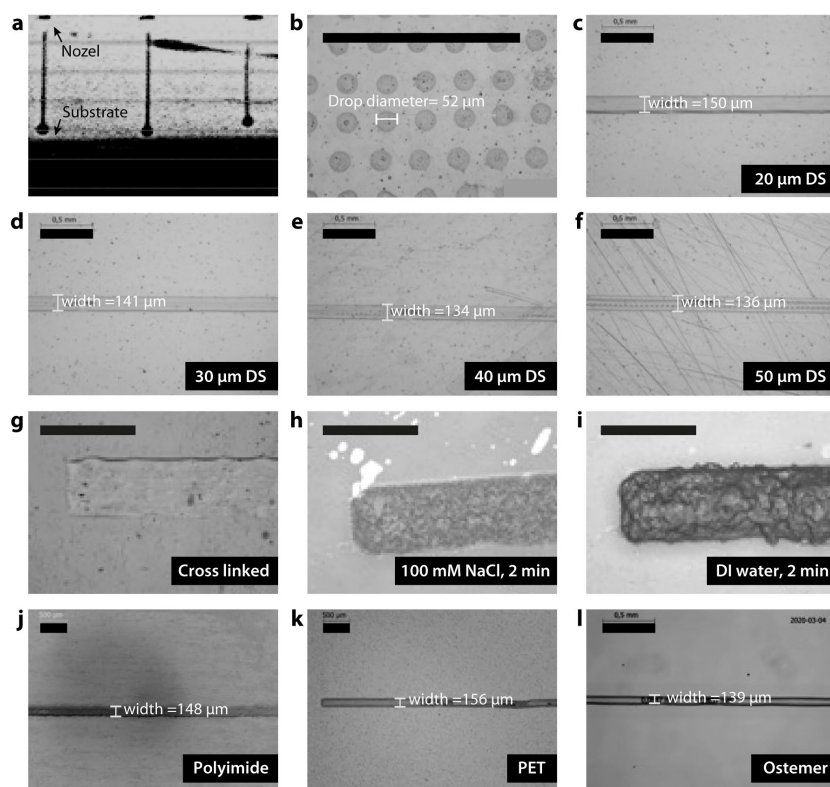
Figure 1. Inkjet printing images of i-AHPG. **a**, Droplet formation at the inkjet nozzle imaged 400 μm from the print head. **b**, Microscope image of i-AHPG printed on PET substrate, droplet spread of 52 μm with 256 μm spacing. **c-f**, Target-width 100 μm line on polyfoil substrate using drop spacing (DS) of 20, 30, 40, and 50 μm. Line width after UV curing measured to be 150, 141, 134, and 136 respectively. **g**, Inkjet printed i-AHPG after UV cross linking and subsequently dipped first, **h**, in 100 mM NaCl for 2 min, and then, **i**, in DI water for 2 min. **j-l**, Target-width 100 μm line printed, after oxygen plasma treatment on polyimide, PET, and Ostemer 221. All scale bars 500 μm

viscosity and modulate the rate of solvent evaporation to facilitate smooth ink flow through the nozzle without drying. Furthermore, temperature variation can decrease particle size, allowing them to pass through the nozzle without obstruction. Through experimentation with various nozzle temperatures for printing i-AHPG ink, it was discovered that clogging could be circumvented by retaining the nozzle temperature at 35 °C. The Supplementary Information contains comprehensive inkjet printing parameters and print waveform settings.

The contact angle is a conventional measurement of the characteristics of the ink droplet on a substrate. High contact angles ($\theta > 90°$) indicates a surface with lower surface energy, resulting in droplets with lower spreading. While lower contact angles ($\theta < 90°$) indicate higher surface energy, resulting in droplets with more spreading.[40] We measured the contact angle of i-AHPG on untreated polyimide substrates to be 58° and resulted in discontinuous i-AHPG prints. To improve ink droplet spread we performed two types of surface treatment: oxygen plasma treatment and application of a surface adhesion promotor PX15 (a UV-curable grafting solution made for creating covalent surface modifications). Both surface treatments reduced the i-AHPG contact angle to a similar value of approximately 25°. This reduction in contact angle resulted in droplets with increased spread that facilitated continuous ink prints (Fig. S2).

Print resolution of i-AHPG was largely determined by two parameters: droplet size (diameter of individual droplets after spreading on the surface) and drop spacing (DS, center-to-center distance between two individual adjacent drops)[34]. Typically, inks utilizing both lower droplet size and DS result in prints of higher resolution. The smallest achievable droplet dispensed for i-AHPG was measured to be 52 μm, indicating the highest possible resolution with the 10 pL cartridge and thus the smallest printable features as observed in Figure 1b. The second parameter, DS, is a critical parameter for the formation of continuous printed layers and strongly influences the thickness of the printed films. Thus,

we performed a systematic study of DS for i-AHPG by varying DS from 20–50 μm while observing the resulting printed layer formation. As can been seen in the microscope images of Figure 1c-d, DS from 20–30 μm resulted in smooth and uniform layer formation. DS greater than 30 μm resulted in discontinuous layers (Figure 1e-f). Another characteristic of the i-AHPG investigated was the so-called property of contact line pinning, the phenomenon whereby the liquid drop edge remains stationary as the solvents evaporate. To have a continuous uniform layer formation we should have good contact line pinning. The optimal drying conditions for various ink types are entirely dependent on their respective formulations. Excessively high temperature can accelerate drying, impeding uniform spreading of the ink, whereas too-low temperatures can hinder complete drying, thereby impacting print quality.[33] We found that for i-AHPG, a plate temperature of 30 °C assisted uniform solvent evaporation and improved contact line pinning and hence uniform layer formation. Altogether, we found an optimized ink recipe with the following printing parameters, used for all results discussed below: 30 μm DS, 30 °C plate temperature, and 35 °C nozzle temperature.

Utilizing the optimized i-AHPG formulation and print recipe we tested i-AHPG for adhesion and crosslinkability. Printed i-AHPG lines were crosslinked by UV curing using a lamp wavelength between 200–400 nm and intensity of 120 W/cm followed by bake in a convection oven at 80 °C to boil off remaining solvent and ensure full crosslinking. The fully cured lines were first dipped in a solution of 100 mM NaCl and then in DI water for 120 s, and subsequently inspected visually using optical microscopy (Figure 1g-i). From these images, it was readily observable that swelling of the printed film occurred due to absorption of water, yet the printed lines were found to be intact and adhered to the substrate during and post hydration. This ink formulation was printed successfully on several commonly used flexible substrates, namely polyethylene terephthalate (PET), polyimide (PI), and Ostemer[41] (Figure 1j-l). From the studies on the formulated i-AHPG for printing, post processing parameters, and adhesion as well as with the proven printability on various substrates, we conclude that the i-AHPG could be adapted to be used in the development of future OEIP devices.

2.2 OEIP fabrication

The fabrication method proposed in this work combines printing of i-AHPG polyelectrolytes on thin polyimide (PI) substrates patterned with common microfabrication protocols to achieve free-standing and flexible OEIPs. We choose PI as the fabrication substrate primarily because the surface energy is compatible with the formulated i-AHPG (promoting good adhesion between the ink and PI) and thin sheets (2–10 μm) of PI can be easily realized via spin casting. Additionally, PI has excellent insulation properties, flexibility, and biocompatibility[42,43] making it a suitable candidate for biomedical and implant applications. The material used for the encapsulation layer was Ostemer 221, a single-UV-cure polymer designed to manufacture high aspect ratio patterns.[44] Ostemer 221 has a chemically reactive thiol group with soft and flexible properties, and when fully cured its Young's modulus is between 5–7 MPa. This enables direct UV patterning of the encapsulation layer without further processing steps or high temperature annealing, such as those needed by PI resins, which may damage the printed PE membrane. We used 4-inch rigid glass wafers as the carrier substrate for ease of handling and high accuracy during each step of the micro-fabrication process.

The fabrication process is depicted in Figure 2 and detailed in the Experimental section below. Briefly, a sacrificial metal adhesion stack (Cr 5 nm followed by Al 50 nm) was thermally evaporated. A base layer of PI was then spin cast and thermally cured. This was followed by an Al alignment layer (thermally evaporated and photolithographically patterned). This layer assisted not only in alignment during fabrication, but additionally enabled visualization under optical microscopy during device positioning for experiments (the i-AHPG ion channel was transparent and not readily visible). The alignment layer was then encased in a second layer of polyimide resin (spin cast). Three parallel lines (55 mm long, between 2.5–3 μm thick via profilometry) of i-AHPG were then printed on the PI surface following the protocol discussed above. The Ostemer 221 encapsulation layer was then wire-bar coated and photolithographically patterned. Openings in the Ostemer encapsulation (60 μm diameter) were patterned at either end of the printed i-AHPG polyelectrolyte lines (perpendicular to the line) providing four inlets and outlets for each line (Figure 3a zoom-ins). An Al hard mask was thermally evaporated and patterned. O_2 plasma etching was then used to remove organic material unprotected by the Al hard
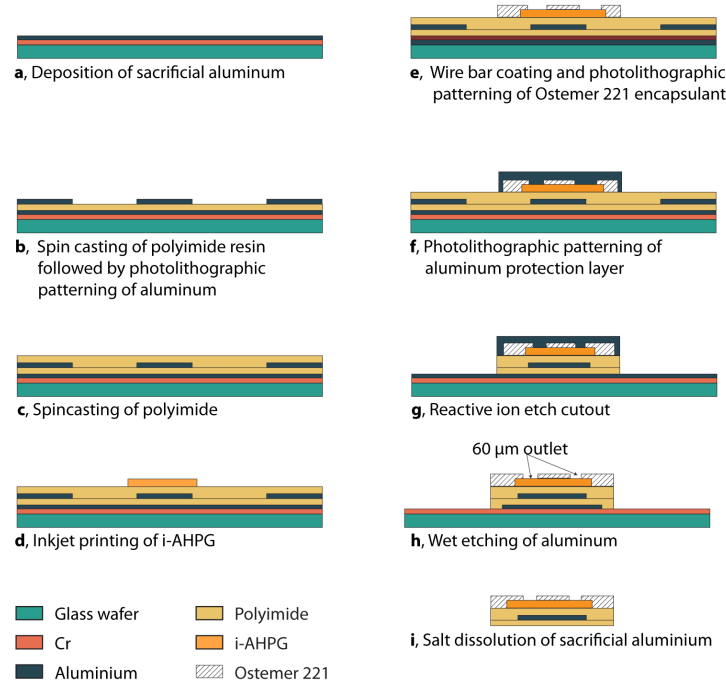
Figure 2. Schematic of fabrication scheme for free standing flexible ion pumps. **a**, Sacrificial adhesion layers thermal evaporated on glass, chromium (5 nm) and aluminum (50 nm). **b**, Spin casting of polyimide resin followed by thermal evaporation and photolithographic patterning of aluminum alignment layer. **c**, Spin casting of polyimide resin encasing aluminum alignment layer. d, Inkjet printing of i-AHPG polyelectrolyte channels. **e**, Wire bar coating and photolithographic patterning encapsulant layer, Ostemer 221 (9 μm) and one step UV-patterning of Ostemer 221 to realize the source and target outlets. **f**, Thermal evaporation and photolithographic patterning of hard etch mask, aluminum (70 nm). **g**, Reactive ion etching of exposed polyimide, separating individual IJ-OEIPs. **h**, Wet etching of aluminum hard mask. **i**, Lift off devices using salt dissolution of sacrificial aluminum layer.

mask. OEIP devices were then lifted off by dissolution (100mM NaCl) of the sacrificial bottom Al layer[45]. The sacrificial Al layer enabled excellent adhesion of the PI substrate during all processing steps and allowed for easily controlled release of the devices. Al dissolution was found to be a quite favorable OEIP processing technique, as it can be performed at room temperature and resulted in gentle release of the final devices. As the PI and Ostemer have lower water transmission rate, the devices were not damaged during the release process. Finally, each individual device was packaged with a heat shrink tube to serve as the source reservoir (as seen in Figure 3c). A schematic and photograph of the patterned PI section of the OEIP are shown in Figure 3a and b, respectively.

2.3 OEIP iontronic characterization

The ionic conductivity in IEMs depends the mobility of the ionic charge carriers. For a CEM such as i-AHPG, the majority of the current through the membrane will be carried by cations from the source reservoir. Hence, the conductivity in the i-AHPG will be mostly dependent on the mobility of the source cation, and less dependent on the target anion. Ions with higher diffusion coefficient will generate higher conductivity as they are transported faster than those with with lower diffusion coefficient. To this aim, four sets of experiments were performed for the OEIPs to measure conductivity for various source and target electrolytes comprising ions of varying diffusion coefficients. To perform each experiment, the OEIP was positioned in a small target reservoir (1 ml Eppendorf tube, Figure 3c) with free-standing PEDOT:PSS source and target electrodes, inside the OEIP shrink-tube reservoir and in the Eppendorf tube, respectively. The four experiments were as follows: (*i*) ion switching (cations with different diffusion coefficient exchanged in source reservoir); (*ii*) target anion switch (anions with different diffusion coefficient exchanged in target); (*iii*) varying source concentration; and (*iv*) evaluation of large(r) ion delivery.
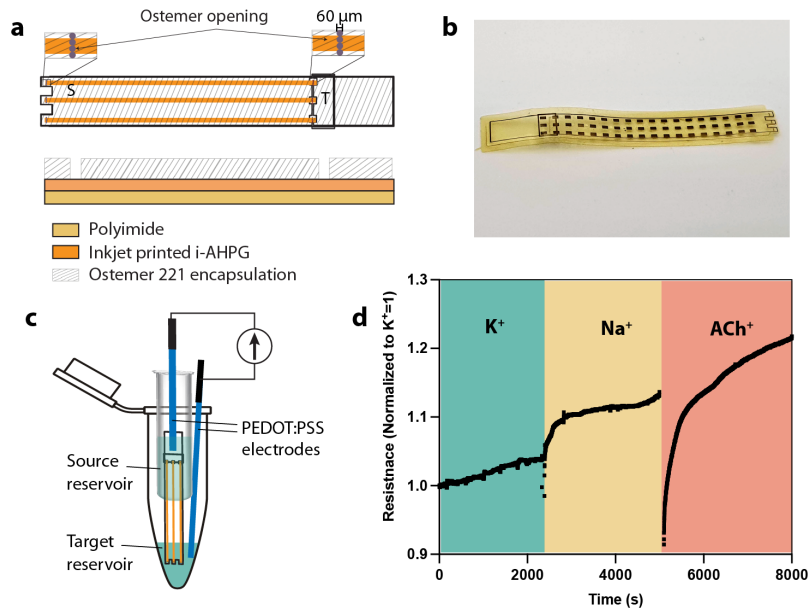
Figure 3. IJ-OEIP characterization. **a**, Device architecture of the IJ-OEIP delivery section showing 4 delivery outlets (60 µm diameter) on each channel (both inlet and outlet). **b**, Photograph of IJ-OEIP delivery section. **c**, Experimental setup for ion exchange characterization using PEDOT:PSS as source and target electrodes. Source reservoir is realized by heat-crimping a tube onto the IJ-OEIP delivery section. **d**, Ionic resistance change when cations in the source reservoir are switched from K^+ to Na^+ to ACh^+, with constant KCl target solution.

In the first experiment to verify basic ion transport capabilities of the OEIP, we delivered various cations at 100 nA by exchanging source reservoir solutions containing 100 mM acetylcholine ACh^+, Na^+, or K^+, with Cl^- as counter ion, and measured the ionic resistance. In all cases the target electrolyte was 100 mM KCl. The resistance of the cations transported scaled inversely with the diffusion coefficients and increased in the order of $K^+ < Na^+ < ACh^+$ (Figure 3d, $D_{K+} = 1.96\times10^{-5}$ cm^{2}s^{-1}, $D_{Na+} = 1.33\times10^{-5}$ cm^{2}s^{-1}, $D_{ACh+} = 0.55\times10^{-5}$ cm^{2}s^{-1})[46,47]. In the second experiment, to elucidate cation selectivity, the anions in the target reservoir were varied by exchanging 100 mM solutions containing Cl^-, $ClO4^-$, Ac^-, with K^+ as counter ion, and source reservoir kept constant with 100 mM KCl. Only a small change in resistance is observed when changing the target electrolyte (Figure S3a), indicating cation selectivity. For the third experiment, the source electrolyte concentration was varied from 1 to 10 to 100 mM KCl (while target electrolyte kept at constant 100 mM KCl). In a selective ionic conductor, with high fixed charge concentration, the ionic conduction should mostly depend on the fixed charge concentration and the cationic mobility in the CEM, rather than the source concentration. Indeed, the ionic resistance showed only small variations on the source concentration (Figure S3a), indicating higher fixed charge concentration, compared to the surrounding electrolytes. Finally, for the fourth experiment evaluating the OEIP's capability to transport larger and more biomedically relevant ions, we used a source electrolyte containing 10 mM bupivacaine HCl. Chemical analysis using a forensic detection kit indicated successful delivery of bupivacaine (Table S2), suggesting that the i-AHPG channel maintained the HPG's capability[4] to transport larger substances on the several 100 g/mol level. Since the OEIPs are essentially ionic resistors, devices were also stress tested by running them at higher currents (200 nA, 500 nA) and recording the device's output resistance as shown in Figure S4.

2.4 In vitro delivery of bupivacaine to DRG cells

The cell bodies of first-order sensory neurons are located in the dorsal root ganglia (DRG) and project axons that bifurcate and thereby connect peripheral structures to the spinal cord. These neurons are responsible for conveying sensory information, including signals acquired from painful stimuli, to the central nervous system for further processing. Bupivacaine, when used as a local anesthetic, exerts its sodium channel blocking function on the peripheral terminals of DRG sensory neurons. Therefore, in these experiments we tested the inkjet-OEIP's utility for bioelectronics applications by delivering
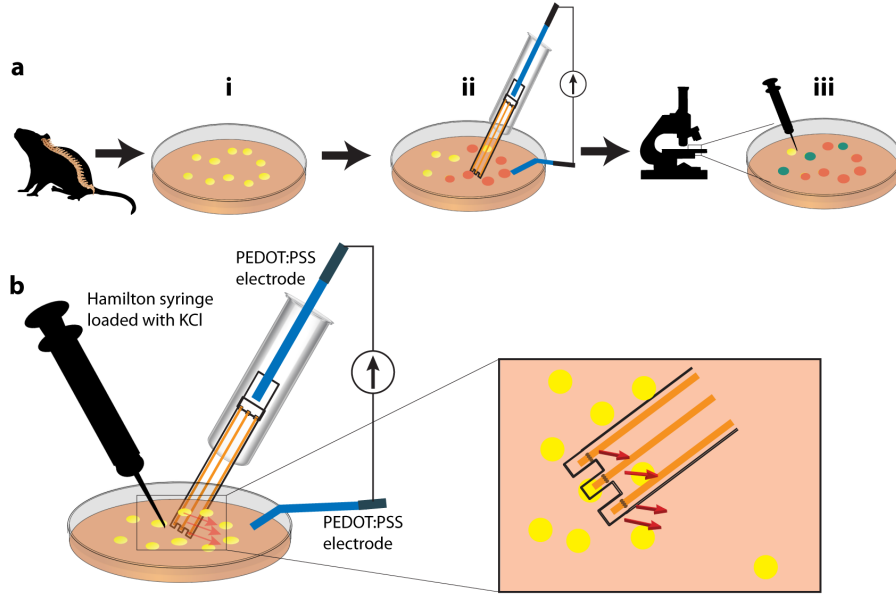
Figure 4. *In vitro* experimental setup. **a**, Overall protocol: **i**, DRGs excised from a naive mouse and further dissociated into cultured cells (in yellow); **ii**, bupivacaine delivered to cells using the IJ-OEIP (orange indicates cells with bupivacaine absorbed); **iii**, K$^+$ delivered to cells and florescence response recorded using confocal microscope and response compared with control dish to see effect of bupivacaine delivery (green indicates cells that did not bind sufficient bupivacaine to significantly decrease their subsequent Ca^{2+} activation). **b**, Focus on in-dish setup. The Hamilton syringe is placed adjacent to the IJ-OEIP delivery point. Close up shows bupivacaine delivery direction towards the cells (red arrows).

bupivacaine to primary mouse DRG cultures *in vitro*. The experimental protocol is visualized in Figure 4. In our setup, the DRG neurons were loaded with a fluorescent calcium indicator (Fluo-3AM) to infer membrane depolarization via intracellular Ca^{2+} flux after administration of KCl. A Hamilton syringe was used to deliver KCl, which promotes DRG depolarization by increasing the extracellular concentration of K$^+$, eventually leading the membrane potential to reach the threshold for Na$^+$ (and subsequently Ca^{2+}) channels to open. Bupivacaine counteracts this activation by binding to the Na$^+$ channels, blocking Na$^+$ influx and preventing depolarization. Thus, successful OEIP mediated delivery of bupivacaine could be demonstrated if the subsequent KCl administration showed *diminished* DRG activation inferred by lower increase of intracellular Ca^{2+} levels. The outlets of the OEIP were oriented downwards towards the cells, allowing bupivacaine delivery to occur in the direction of the cells (red arrows in Fig. 4).

Varying amounts of bupivacaine were delivered (reported as summed charge in Fig. 5), and the cell response was studied at varying distances from the delivery point to understand the spatial precision capabilities of the OEIP in this setting. After delivery of bupivacaine at 500 nA at 1, 2.5, and 20 min, equivalent to 30, 75, and 600 µC (integrated current) respectively, 3 µL of 50 mM KCl was delivered locally to the cells via the Hamilton syringe. The intracellular levels of Ca^{2+} were recorded as an increase of the fluorescence signal using a confocal microscope. For the cell analysis, we divided the microscope view into 2 different regions of interest (Figure 5a). Area 1 was defined below the delivery outlets and area 2 was defined away from the outlets. The cell response in areas 1 and 2 to KCl after the various amounts of delivered bupivacaine, as well as control response to no bupivacaine, is shown in Figure 5c and d. Particularly in area 1, the cells responded as expected for successful bupivacaine delivery: the fluorescence response upon KCl delivery was reduced by the bupivacaine. In area 2, ~120 µm away from closest delivery outlet, the effect of bupivacaine was less observable. Transport of bupivacaine beyond the OEIP outlet is highly limited to diffusive flow in the space between the OEIP and the petri dish and, without convection by fluidic movement, the concentration rapidly falls with distance from the outlet. For this reason, we see a much weaker effect in area 2. The difference in area 1 and 2 responses indicates that the OEIP can readily deliver bupivacaine, a potent pharmaceutical compound, with high (~100 µm) spatial resolution. Interestingly, the effect of bupivacaine delivery appears to saturate already
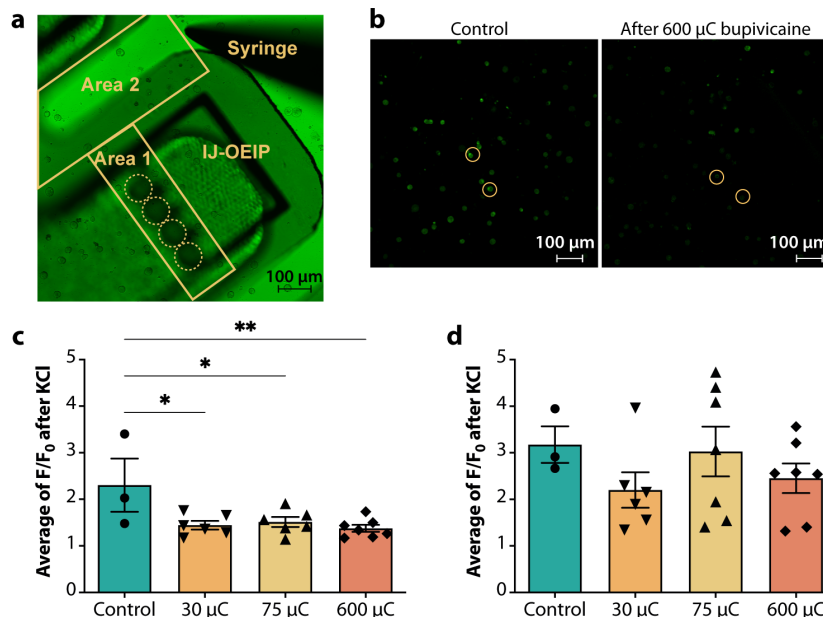
Figure 5. IJ-OEIP delivery of bupivacaine *in vitro*. **a**, Microscope image showing the IJ-OEIP, Hamilton syringe tip, and analysis areas 1 and 2. The 60μm diameter outlets are marked with dotted circles. **b**, Florescence imaging of the area under analysis (after 3 μL KCl): left, no bupivacaine delivery (control), and right, after 600 μC bupivacaine delivery. Two cells in area 1 are annotated in both images as an example for each case. **c,d**, Cell response after KCl delivery vs different amounts of bupivacaine delivered for (**c**) area 1 and (**d**) area 2 (n = 3-4 mice, N = 3-6 dishes).

at the shortest delivery duration (500 nA for 1 min, or 30 μC), indicating that future implementations of OEIP-based therapies could be optimized with very low dosages.

3. Conclusions

Here we report the development of a formulation of printable and UV-curable PE ink, i-AHPG, based on anionic functionalized hyperbranched polyglycerol. The physical characteristics related to this PE ink's stability and print characteristics on polymer substrates are studied. Utilizing an optimized formulation of i-AHPG, we establish a hybrid micro-processing and inkjet-printing protocol to produce free standing, flexible inkjet-OEIPs. The performance of the i-AHPG PE membrane is studied for these OEIP devices in a series of ion transport experiments. In these experiments, the voltage and current values are recorded from OEIP devices during the loading, transport, and delivery using various ionic concentrations and species in the source and target reservoirs. Further, utilizing a forensic test kit, we confirm the ability of i-AHPG PE membranes to transport the pharmaceutical compound bupivacaine, a widely used amide-type, long acting, local anesthetic on the World Health Organization's List of Essential Medicines. Finally, OEIPs are used in the successful targeted delivery of bupivacaine to primary murine DRG neurons. In these fluorescent cell studies, we were able to reliably elicit strong cell response to bupivacaine delivery near the OEIP channel outlets (within a radius of ~120 μm), while cells further away appear essentially unaffected. These results highlight the spatial precision and bupivacaine delivery capability of the OEIP and have positive implications for iontronics targeted towards application in pain therapies.

The i-AHPG ink reported here together with additive inkjet printing methodology is adaptable to many iontronic technologies and offers a significant simplification in fabrication protocols, as well as widening the range of available device architectures. While an important first step, we anticipate further progress to be made in the area of printable iontronics, for example in the development of corresponding cationic functionalized ink, eco/bio-friendly ink formulations with less/no methanol, printed iontronic devices integrated with other systems, fully printed devices, and 3D printed iontronic device

architectures. Only through continued improvements to the employed fabrication methods can the aims of seamless electronic to ionic interaction with living systems be achieved.

4. Experimental

Inkjet formulation

The dendrolyte AHPG was synthesized according to a previously reported process[25]. AHPG (25 wt%) was mixed with Thiocure ETTMP 1300 (5wt%, Bruno Bock), Irgacure 2959 (0.5 wt%, Sigma- Aldrich), methanol (39 wt%), and water (29 wt%) and vortexed for 10 min or until all the AHPG powder was dissolved. After filtering this mixture with a 0.45 μm PVDF filter, a liquid polymer-based surfactant and defoamer (1.5 wt%, Nuosperse 2008, Elementis) was added to the mixture. The solution was used within a period of 12 h after blending. Longer storage times led to particulates that could clog to the inkjet nozzles.

OEIP fabrication and operation

All devices were fabricated on 4-inch glass wafers (Specialty Glass Products). The glass wafers were cleaned, rinsed using Acetone and DI water, then vacuum hot plate baked (110 °C, 90s). A 5 nm layer of Ti/Cr was thermally evaporated on the glass wafer followed by a 50 nm aluminum evaporation. Polyimide (PI2611, HD Microsystems) was spincoated (2000 rpm, 30 s) on top of the aluminum-deposited glass wafers and cured under nitrogen (N_2) (ramp 3 °C/min until 300 °C, hold 300 °C for 30 min). Another layer of 50 nm aluminum was evaporated followed by spin coating S1818 (4000 rpm, 30 s), vacuum plate baked (110 °C, 90 s), UV exposed (10 s) using mask aligner (MA6-BA6 Karl Süss), developed using MF319 (≤30 s), etched with aluminum etchant (at 42 °C), and S1818-stripped with acetone. Then the polyimide spin coating and curing step explained before was repeated. PX15 (Mercenelabs), a polymer-bonding surface modifier, was applied directly on the wafer (manually using clean room gloves) followed by 120 s UV exposure. This formed a monolayer of PX15 and the rest of the PX15 was removed with isopropanol.

The inkjetting process began by filling a 10 pl (DMC-11610) Dimatix cartridge with the i-APHG formulation using a 5 or 10 ml plastic syringe. i-AHPG was then inkjet printed (Dimatix 2831) at 25 μm drop spacing, 28 °C platen temperature, 35 °C nozzle temperature, and 20-25 V voltage (see Supplementary Information for full details). The waveform (Figure S1) used for this material was optimized to get the best drop formation for our formulation. Regular cleaning cycles were also introduced to avoid nozzle clogging. The inkjet printing was done within a period of 6 h after PX15 deposition. The printed wafers were subsequently encapsulated and patterned (to reveal the inlet and outlet of the ion pump) using Ostemer 221 (Mercenelabs), a commercially available single UV curable polymer. The Ostemer 221 was wire bar coated, wet exposed for 12 s, developed with butyl acetate, and oven baked at 110 °C for 12 h. A 70 nm aluminum layer was thermally evaporated followed by S1818 spin coating, exposing (10 s) using mask aligner (MA6-BA6 Karl Süss), developed with MF319 (≤30 s), etched (aluminum etchant ≤120 s), and finally S1818-stripped using acetone. The wafer was then subjected to reactive ion etching (O_2 100 sccm, CF4 200 sccm, 300 W, 2400 s, Advanced Vacuum Reactive), to form the desired device patterns. Finally, the wafer was kept in aluminum etchant heated to 42 °C for 120 s, to remove the top aluminum layer, followed by keeping the wafer in 10 mM NaCl for at least 72 h to peel off fully flexible ion pumps on polyimide.

All OEIP devices were operated using a Keithley 2600 series SourceMeter controlled via a custom LabVIEW program.

Dorsal root ganglia (DRG) cell culture

DRGs cultures were prepared using a modified version of the protocol described by Malin, et al.[48]. In brief, DRG (C1-L6) from BALB/c female mice (12-14 weeks of age) were dissected and kept in cold HBSS (without calcium and magnesium; Gibco) until enzymatically dissociated first with papain (60U; 30 min at 37 °C; Worthington) followed by a mix of collagenase II and dispase II (12 and 14 mg/ml

respectively; 30 min at 37 °C; Worthington and Sigma, respectively). DRG cells were then gently triturated in F12 media (Gibco) added with 1% penicillin and streptomycin (Thermo Fisher Scientific) and 10% heat-inactivated fetal bovine serum (FBS; Gibco). Finally, cells were plated in glass bottom dishes (Mattek) previously coated with poly-D-lysine and laminin (Corning and Sigma, respectively) and then maintained in 5% CO_2 environment at 37 °C until the next day for the scheduled calcium imaging experiments. All the experiments were approved by the local ethics committee for animal experiments in Sweden (Stockholm Norra Djurförsöksetiska nämnd).

Calcium imaging

The calcium indicator Fluo-3AM (4.4 µM; Thermo Fisher Scientific) in modified Hepes buffer (10 mM Hepes, 2 mM $CaCl_2$, 3 mM KCl, 145 mM NaCl, 2 mM $MgCl_2$, 10 mM glucose; brought to pH 7.4 using NaOH) was used for monitoring intracellular levels of calcium in DRG neurons after 24 h in culture. Incubation with the calcium dye was carried out for 30 min at 37 °C and then modified Hepes buffer was used to wash the cells. Cells were subsequently positioned under a Zeiss LSM800 confocal microscope for the experiments. A 10× objective and an argon laser (488 nm excitation) were used for performing calcium imaging.

The day before the calcium imaging experiment, a 100 mM bupivacaine solution was loaded into the OEIP shrink tube reservoir along with an anodic PEDOT:PSS electrode. An analogous cathodic PEDOT:PSS electrode was submerged in an Eppendorf with modified Hepes buffer, which replicates the extracellular environment salt concentration level (Figure 3c). The loading of bupivacaine was driven by applying a constant current of 10 nA for at least 12 hours. For the control, the OEIP was not loaded with bupivacaine the previous day.

For the calcium imaging experiment, a cathodic PEDOT:PSS electrode was put at the edge of the petri dish containing the cells and the OEIP (loaded overnight) was positioned manually using a micromanipulator close to the cells (Figure 4b). OEIP delivery outlets were arranged with a vertical distance from the cells (seeded at the bottom of the petri dish) of around 90–130 µm. This distance range was chosen to enable proximate delivery of bupivacaine to the cells. The OEIP was then activated with 500 nA current for 1, 2.5, or 20 min to deliver bupivacaine to the cells. Afterwards, the Hamilton syringe previously positioned using a micro manipulator in the contiguity with the OEIP was used to deliver 3 µL of 50 mM KCl to the cells.

The variation in emission (506 nm), induced by the binding of intracellular calcium to Fluo-3AM, was measured every 2.5 s using a photomultiplier tube. The acquired images pre- (10) and post-KCl application (90) were analyzed using ImageJ software. In each image, the mean fluorescence intensity (F) of each neuron was measured manually by selecting all the cells present in the field of image and dividing them into different areas (closer to the outlets delivering bupivacaine and further away, respectively area 1 and 2). The baseline recording (F_0) of each neuron was calculated as the average mean signal of the initial 10 images of the series before KCl was applied. Data are presented as the average of max F/F_0 per dish.

Statistical analysis

In calcium imaging experiments, for comparing differences in fluorescence with three or more groups, one-way ANOVA was used, followed by Dunnet post hoc test. P values <0.05 were considered significant.

Acknowledgements

Conflict of interest

A.R., A.B.F., T.A., T.A.S., K.T., D.N., M.B., C.I.S., D.J.P., and D.T.S. are shareholders in the small, researcher-controlled intellectual property company OBOE IPR AB (oboeipr.com), which owns the patents related to the ion pumps presented above. All other authors declare no conflict of interest.

References

[1]   K. Xiao, C. Wan, L. Jiang, X. Chen, M. Antonietti, *Adv. Mater.* **2020**, 2000218.

[2]   A. Armgarth, S. Pantzare, P. Arven, R. Lassnig, H. Jinno, E. O. Gabrielsson, Y. Kifle, D. Cherian, T. Arbring Sjöström, G. Berthou, J. Dowling, T. Someya, J. J. Wikner, G. Gustafsson, D. T. Simon, M. Berggren, *Sci. Rep.* **2021**, *11*, 7757.

[3]   D. T. Simon, E. W. H. Jager, K. Tybrandt, K. C. Larsson, S. Kurup, A. Richter-Dahlfors, M. Berggren, in *IEEE TRANSDUCERS 2009*, IEEE, **2009**, pp. 1790–1793.

[4]   D. J. Poxson, E. O. Gabrielsson, A. Bonisoli, U. Linderhed, T. Abrahamsson, I. Matthiesen, K. Tybrandt, M. Berggren, D. T. Simon, D. J. Poxson et al., *ACS Appl. Mater. Interfaces* **2019**, *11*, 14200.

[5]   C. M. Proctor, A. Slézia, A. Kaszas, A. Ghestem, I. del Agua, A.-M. Pappa, C. Bernard, A. J. Williamson, G. G. Malliaras, *Sci. Adv.* **2018**, *4*, eaau1291.

[6]   L. Waldherr, M. Seitanidou, M. Jakešová, V. Handl, S. Honeder, M. Nowakowska, T. Tomin, M. Karami Rad, T. Schmidt, J. Distl, R. Birner‑Gruenberger, G. Campe, U. Schäfer, M. Berggren, B. Rinner, M. Asslaber, N. Ghaffari‑Tabrizi‑Wizsy, S. Patz, D. T. Simon, R. Schindl, *Adv. Mater. Technol.* **2021**, *6*, 2001302.

[7]   D. J. Poxson, M. Karady, R. Gabrielsson, A. Y. Alkattan, A. Gustavsson, S. M. Doyle, S. Robert, K. Ljung, M. Grebe, D. T. Simon, M. Berggren, *Proc. Natl. Acad. Sci.* **2017**, *114*, 4597.

[8]   D. T. Simon, S. Kurup, K. C. Larsson, R. Hori, K. Tybrandt, M. Goiny, E. W. H. Jager, M. Berggren, B. Canlon, A. Richter-Dahlfors, *Nat. Mater.* **2009**, *8*, 742.

[9]   D. Cherian, A. Armgarth, V. Beni, U. Linderhed, K. Tybrandt, D. Nilsson, D. T. Simon, M. Berggren, *Flex. Print. Electron.* **2019**, *4*, 022001.

[10]   C. M. Proctor, I. Uguz, A. Slezia, V. Curto, S. Inal, A. Williamson, G. G. Malliaras, *Adv. Biosyst.* **2019**, *3*, 1800270.

[11]   T. Arbring Sjöström, A. I. Ivanov, C. Bernard, K. Tybrandt, D. J. Poxson, D. T. Simon, M. Berggren, *Adv. Mater. Technol.* **2021**, *6*, 2001006.

[12]   E. O. Gabrielsson, K. Tybrandt, M. Berggren, *Lab Chip* **2012**, *12*, 2507.

[13]   E. O. Gabrielsson, K. Tybrandt, M. Berggren, *Biomicrofluidics* **2014**, *8*, 064116.

[14]   T. Arbring Sjöström, M. Berggren, E. O. Gabrielsson, P. Janson, D. J. Poxson, M. Seitanidou, D. T. Simon, *Adv. Mater. Technol.* **2018**, *3*, 1700360.

[15]   J. Kamcev, D. R. Paul, B. D. Freeman, *J. Mater. Chem. A* **2017**, *5*, 4638.

[16]   A. J. Williamson, J. Rivnay, L. Kergoat, A. Jonsson, S. Inal, I. Uguz, M. Ferro, A. Ivanov, T. A. Sjöström, D. T. Simon, M. Berggren, G. G. Malliaras, C. Bernard, *Adv. Mater.* **2015**, *27*, 3138.

[17]   N. Abdullayeva, M. Sankir, *Materials (Basel).* **2017**, *10*, 586.

[18]   A. Jonsson, S. Inal, I. Uguz, A. J. Williamson, L. Kergoat, J. Rivnay, D. Khodagholy, M. Berggren, C. Bernard, G. G. Malliaras, D. T. Simon, *Proc. Natl. Acad. Sci.* **2016**, *113*, 9440.

[19]   H. L. Gomes, M. C. R. Medeiros, F. Villani, J. Canudo, F. Loffredo, R. Miscioscia, C. Martinez-Domingo, E. Ramon, E. Sowade, K. Y. Mitra, R. R. Baumann, I. McCulloch, J. Carrabina, *Microelectron. Reliab.* **2015**, *55*, 1192.

[20]   D. Cherian, K. Y. Mitra, M. Hartwig, P. E. Malinowski, R. R. Baumann, *IEEE Sens. J.* **2018**, *18*, 94.

[21]   K. Y. Mitra, E. Sowade, C. Martínez-Domingo, E. Ramon, J. Carrabina, H. L. Gomes, R. R. Baumann, *AIP Conf. Proc.* **2015**, *1646*, 106.

[22]   E. T. S. G. da Silva, S. Miserere, L. T. Kubota, A. Merkoçi, *Anal. Chem.* **2014**, *86*, 10531.

[23]   G. Kollamaram, S. C. Hopkins, B. A. Glowacki, D. M. Croker, G. M. Walker, *Eur. J. Pharm. Sci.* **2018**, *115*, 248.

[24]   A. Negro, T. Cherbuin, M. P. Lutolf, *Sci. Rep.* **2018**, *8*, 17099.

[25]   T. Abrahamsson, M. Vagin, M. Seitanidou, A. Roy, J. Phopase, I. Petsagkourakis, N. Moro, K. Tybrandt, X. Crispin, M. Berggren, D. T. Simon, *Polymer (Guildf).* **2021**, *223*, 123664.

[26]   T. Abrahamsson, D. J. Poxson, E. O. Gabrielsson, M. Sandberg, D. T. Simon, M. Berggren, *Front. Chem.* **2019**, *7*, 484.

[27]   T. Arbring Sjöström, A. Jonsson, E. Gabrielsson, L. Kergoat, K. Tybrandt, M. Berggren, D. T. Simon, *ACS Appl. Mater. Interfaces* **2017**, *9*, 30247.

[28]   E. O. Gabrielsson, M. Berggren, *Biomicrofluidics* **2013**, *7*, 64117.

[29]   D. C. Moor, L. D. Bridenbaugh, G. E. Thompson, R. I. Balfour, W. G. Horton, *Anesth. Analg.* **1978**, *57*, 42.

[30]   A. Casati, M. Putzu, *Best Pract. Res. Clin. Anaesthesiol.* **2005**, *19*, 247.

[31]   M. Singh, H. M. Haverinen, P. Dhagat, G. E. Jabbour, *Adv. Mater.* **2010**, *22*, 673.

[32]   S. Jung, A. Sou, K. Banger, D.-H. Ko, P. C. Y. Chow, C. R. McNeill, H. Sirringhaus, *Adv. Energy Mater.* **2014**, *4*, 1400432.

[33]   I. M. Hutchings, G. D. Martin, *Inkjet Technology for Digital Fabrication*, C 2013 John Wiley & Sons Ltd, **2013**.

[34]   M. Singh, H. M. Haverinen, P. Dhagat, G. E. Jabbour, *Adv. Mater.* **2010**, *22*, 673.

[35]   B. J. de Gans, P. C. Duineveld, U. S. Schubert, *Adv. Mater.* **2004**, *16*, 203.

[36]   W. Heller, M.-H. Cheng, B. W. Greene, *J. Colloid Interface Sci.* **1966**, *22*, 179.

[37]   Fujifilm, "Dimatix Materials Cartridge – Samba Cartridge," can be found under https://asset.fujifilm.com/www/us/files/2021-04/ae8a1e167ce8c273fcdd31ecffd9ec80/PDS00142.pdf, **n.d.**

[38]   Dataphysics Instruments, "Surface tension values of some common test liquids for surface energy analysis," can be found under https://www.dataphysics-instruments.com/Downloads/Surface-Tensions-Energies.pdf, **n.d.**

[39]   F. Zhang, C. Tuck, R. Hague, Y. He, E. Saleh, Y. Li, C. Sturgess, R. Wildman, *J. Appl. Polym. Sci.* **2016**, *133*, 43361.

[40]   S.-H. Lee, Y.-J. Cho, *J. Electr. Eng. Technol.* **2012**, *7*, 91.

[41] D. Sticker, S. Lechner, C. Jungreuthmayer, J. Zanghellini, P. Ertl, *Anal. Chem.* **2017**, *89*, 2326.

[42] A. J. T. Teo, A. Mishra, I. Park, Y.-J. Kim, W.-T. Park, Y.-J. Yoon, *ACS Biomater. Sci. Eng.* **2016**, *2*, 454.

[43] C. P. Constantin, M. Aflori, R. F. Damian, R. D. Rusu, *Mater. 2019, Vol. 12, Page 3166* **2019**, *12*, 3166.

[44] Ostemers, "Ostemer 220 Litho," can be found under https://www.ostemers.com/products/ostemer-litho/, **n.d.**

[45] S. Metz, A. Bertsch, P. Renaud, *J. Microelectromechanical Syst.* **2005**, *14*, 383.

[46] P. Vanýsek, in *CRC Handb. Chem. Physics, Ed. 91*, **1996**, pp. 5–98.

[47] E. M. Sega, C. F. Tormena, P. R. de Oliveira, R. Rittner, L. W. Tinoco, J. Figueroa-Villar, N. F. Höehr, *J. Mol. Struct.* **2006**, *797*, 44.

[48] S. A. Malin, B. M. Davis, D. C. Molliver, *Nat. Protoc.* **2007**, *2*, 152.

Supplementary information

Flexible organic electronic ion pump fabricated using inkjet printing and microfabrication for precision *in vitro* delivery of bupivacaine

Table S1. Dimatix 2831 inkjet printing and nozzle settings.

Substrate temperature	Active nozzles	Jetting Voltage	Meniscus Vacuum	Print head height
30 °C	4-8	24	3-inch H_2O	0.500 mm

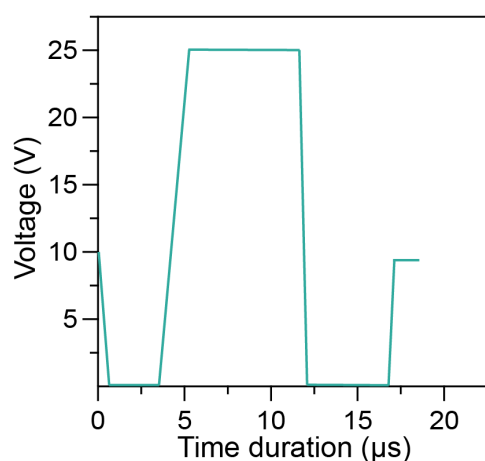| Nozzle temperature	Nozzle number	Nozzle diameter	Drop volume	Jetting Frequency
35 °C	16	21 µm	10 pL	60 Hz

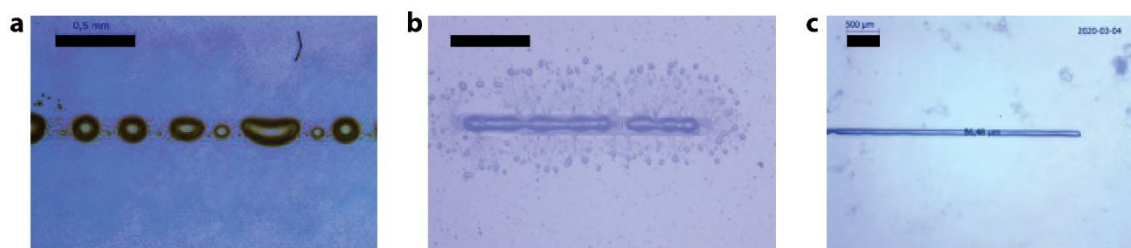**Figure S1.** Optimized voltage waveform used for printing.

Figure S2. a, Optimized ink printed on untreated substrate. **b**, Unoptimized printed lines and influence of satellite drops on treated substrate. **c**, Optimized ink printed on PET substrate.
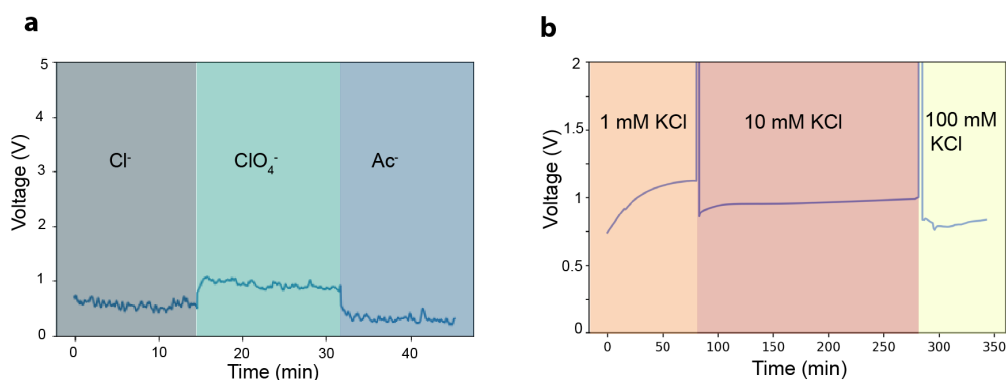

Figure S3. Voltage changes at constant current (100 nA). **a**, When anions in the target solution are subsequently switched between Cl^-, ClO_4^-, and Ac^-, while keeping source electrolyte KCl constant. **b**, When concentration of the source KCl solution is switched in the sequence 1 mM, 10 mM, 100 mM while keeping the target electrolyte concentration constant at 100 mM KCl.

Bupivacaine estimation

Preliminary estimation of bupivacaine was performed using ELISA (enzyme linked immunosorbent assay) (Neogen Mepivacaine forensic kit) where quantification is based on the analyte's (bupivacaine's) ability to compete for the limited number of available specific binding sites along with the horseradish peroxidase enzyme conjugate. The supplier-specified protocol was followed for the estimation. Table S3 shows the absorption data of the analytes sampled from 2 devices after transporting bupivacaine with a constant current of 100 nA for 12 hours. The test verified the delivery of bupivacaine using the devices we fabricated.

Table S2. Absorption measurement data for ELISA (blue corresponds to intensity of absorption).

Dilution Series	Device 1	Device 2
1×	0.073	0.126
10×	0.082	0.221
50×	0.104	0.115
100×	0.106	0.097
200×	0.198	0.148
DI water*	0.401	0.424
Positive control*	0.086	0.29
Negative control*	0.542	0.599

*To verify the viability of the kit

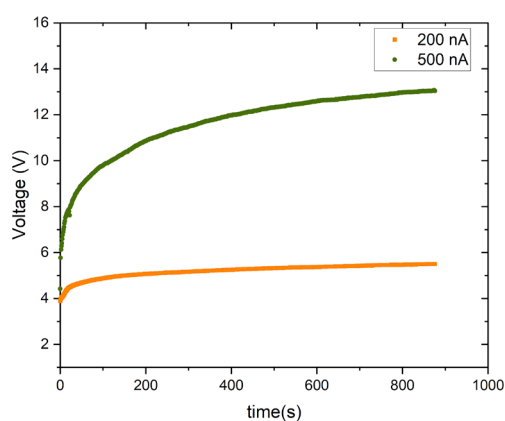## Effect of OEIP resistance at different applied currents

Figure S4. Effect of OEIP output voltage (/resistance) at applied currents of 200 nA (orange curve) and 500 nA (green curve) while delivering bupivacaine molecules to extracullular solution (EC)